J. Fluid Mech. (2020), *vol.* 887, A30. © The Author(s), 2020.
Published by Cambridge University Press
doi:10.1017/jfm.2020.15

Controlled stationary/travelling cross-flow mode interaction in a Mach 6.0 boundary layer

Alexander Arndt[1], Thomas Corke[1,†], Eric Matlis[1] and Michael Semper[2]

[1]University of Notre Dame, Institute for Flow Physics and Control, Aerospace and Mechanical Engineering Department, Notre Dame, IN 46556, USA

[2]US Air Force Academy, Colorado Springs, CO 80840, USA

(Received 16 August 2019; revised 20 December 2019; accepted 28 December 2019)

Experiments were performed to further investigate a quadratic interaction between stationary and travelling cross-flow modes that was revealed in the previous experiment by Corke *et al.* (*J. Fluid Mech.*, vol. 856, 2018, pp. 822–849) in the boundary layer on a sharp right-circular cone at an angle of attack at Mach 6.0. As with the previous experiment, passive discrete roughness was applied near the cone tip, just upstream of Branch I of the linear stability neutral curve for stationary cross-flow modes. The passive roughness consisted of indentations (dimples) that were evenly spaced azimuthally to excite a specific azimuthal wavenumber. A plasma actuator was located just downstream of the discrete roughness array. This was designed to produce an azimuthally uniform unsteady disturbance with a frequency that was at the centre of the band of most amplified travelling cross-flow modes. Measurements consisted of off-wall azimuthal profiles of mean and fluctuating total pressure at different axial locations. Spectra of total-pressure fluctuations verified the receptivity of the boundary layer to the unsteady excitation. This affected the azimuthal and streamwise development of the stationary cross-flow modes, with a general effect to move the transition location upstream by approximately 16 %. The quadratic interaction between the stationary and travelling cross-flow modes was further enhanced by the excitation of the travelling cross-flow mode. This was particularly evident by an enlarged band of azimuthal wavenumbers over which a significant triple phase locking existed. The significantly enlarged range of wavenumber sum and difference interactions offered a mechanism for rapid spectral broadening that could account for the hastened transition by the addition of unsteady disturbances.

Key words: high-speed flow, boundary layer stability, transition to turbulence

1. Introduction

Transition to turbulence on hypersonic lifting bodies is likely to be dominated by a mean cross-flow velocity component that is subject to a cross-flow instability. The first stage of cross-flow instability dominated transition starts with the process of receptivity (Morkovin 1990*a*,*b*; Saric, Reed & Kerschen 2002; Reshotko 2008).

† Email address for correspondence: tcorke@nd.edu

https://doi.org/10.1017/jfm.2020.15 Published online by Cambridge University Press

Based on linear stability theory, travelling cross-flow modes are more amplified than stationary cross-flow modes. However, the stationary modes are highly receptive to surface roughness, which can provide higher initial amplitudes that compensate for their lower amplification rate. As a result, except in instances of higher free-stream turbulence levels (Bippes 1999), the stationary modes are the leading mechanism in cross-flow dominated transition.

As stationary cross-flow modes grow in amplitude, they form co-rotating vortices. As a result of their approximate alignment with the inviscid streamlines of the baseline flow, the vortices have a strong integrated effect on the boundary layer. As they reach larger amplitudes, the stationary cross-flow modes produce a mean flow distortion that includes the formation of an inflected mean velocity profile (Malik, Li & Chang 1994; Malik *et al.* 1999; Chernoray *et al.* 2005; White & Saric 2005) that is inviscidly unstable, and can lead to rapid breakdown. Turbulent transition originating from a cross-flow instability is presented in a number of comprehensive reviews by Reed & Saric (1989), Wassermann & Kloker (2002), Saric, Reed & White (2003) and Bonfigli & Kloker (2007).

The approach to control cross-flow transition stems from the extreme receptivity of the stationary modes to surface roughness. This feature was exploited by Corke & Knasiak (1998) and Corke, Matlis & Othman (2007) to excite selected wavenumbers of cross-flow modes in the boundary layer over a rotating disk, which is a canonical three-dimensional flow that exemplifies the cross-flow instability. Saric, Carillo & Reibert (1998) and Radeztsky, Reibert & Saric (1999) exploited this property in their swept wing experiments to excite fixed spanwise wavenumber stationary cross-flow modes using arrays of micron-sized circular distributed roughness elements. They demonstrated that stationary cross-flow modes at the forced spanwise wavenumber exclusively appeared in the boundary layer.

The ability to excite specific wavenumbers of stationary cross-flow modes led to the concept for cross-flow transition control where roughness is used to excite less amplified stationary modes (Saric *et al.* 1998). The intent is to bias the natural selection mechanism by raising the initial amplitude of a less amplified stationary cross-flow mode so that it initially dominates and inhibits the growth of the more amplified stationary mode. Defining the most amplified wavenumber of the stationary cross-flow mode as the 'critical' wavenumber, Radeztsky *et al.* (1999) investigated discrete roughness for transition control with a 1.5 times larger wavenumber, which they termed 'subcritical' roughness. The approach was shown to substantially increase the transition Reynolds number on a swept wing model in wind tunnel experiments (Saric *et al.* 1998; Saric & Reed 2002). However, more recently (Saric *et al.* 2019), high Reynolds number flight experiments on a swept wing failed to produce a significant delay in transition.

Schuele, Corke & Matlis (2013) investigated discrete roughness for cross-flow transition control on a sharp-tipped right-circular cone at an angle of attack in a supersonic flow. The experiments were performed in the Mach 3.5 supersonic low disturbance tunnel (SLDT) at the NASA Langley Research Center that is specially designed to minimize acoustic disturbances. It documented a 40 % increase in the transition Reynolds number with 'subcritical' wavenumber roughness compared to that with 'critical' wavenumber roughness.

More recently, Corke *et al.* (2018) utilized the Schuele *et al.* (2013) cone model in a Mach 6.0 flow. The cone was placed at a 6° angle of attack (compared to 4.2°) so that the most amplified ('critical) wavenumber of the stationary cross-flow mode, and Branch I location, were the same as that at the lower Mach number. This allowed the

https://doi.org/10.1017/jfm.2020.15 Published online by Cambridge University Press

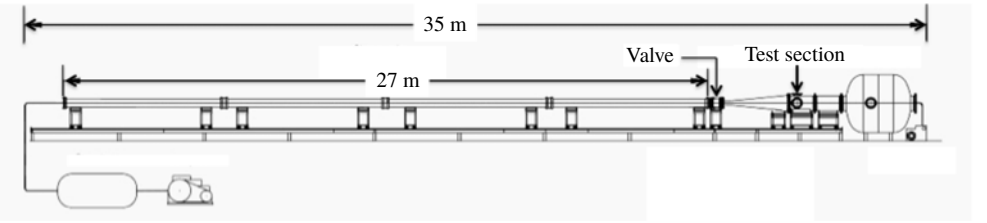


FIGURE 1. Schematic of US Air Force Academy Mach 6.0 Ludwieg Tube where the experiments were performed. From Cummings & McLaughlin (2012).

same discrete roughness cone tips to be used. Besides the Mach number difference, the experiment was conducted in a conventional (non-quiet design) wind tunnel.

In these experiments, the 'subcritical' roughness was found to increase the transition Reynolds number by approximately 25 % compared to the 'critical' wavenumber roughness. Given that the roughness design was the same in both experiments, the poorer performance compared to that of Schuele *et al.* (2013) was speculated to be due to (i) the difference in Mach numbers, or (ii) the difference in the acoustic disturbance levels between the experiments.

Coupled with these results was evidence of a quadratic interaction between the stationary and travelling cross-flow modes. This was confirmed using the cross-bicoherence statistic that documented triple wavenumber phase locking between these modes.

The observation of the quadratic interaction between the stationary and most amplified travelling cross-flow modes, and the speculation that the lower degree of transition suppression was the result of higher acoustic disturbance levels in the conventional (non-quiet) tunnel prompted a follow-on experiment in which the amplitude of the travelling modes might be directly varied. The general objectives were then to

(*a*) seek to control the initial amplitude of the travelling cross-flow modes, while at the same time introducing controlled stationary cross-flow modes;
(*b*) document the effect this had on the nonlinear interaction between stationary and travelling cross-flow modes and spectral broadening; and
(*c*) document the overall effect that the travelling mode initial amplitude had on the transition Reynolds number.

2. Experimental set-up

As in the previous work (Corke *et al.* 2018), the experiments were conducted in the Air Force Academy (AFA) Mach 6.0 Ludwieg Tube Facility. The facility is based on the design used in the Technical University at Braunschweig, Germany (Estorf, Wolf & Radespiel 2005). A schematic of the facility is shown in figure 1. It consists of a 27 m long charge tube that is heated and insulated. The pressurized tube discharges through a converging–diverging nozzle from which a Mach 6.0 flow exits into an open-jet test section. A fast-acting plunger valve is located just upstream of the nozzle throat. When the valve opens, an unsteady expansion wave travels both upstream and downstream. The upstream moving expansion wave reflects at the end of the charge tube and then travels downstream until it reaches the nozzle. The time for this sets the duration of quasi-steady flow conditions in the nozzle and the hypersonic test section.

https://doi.org/10.1017/jfm.2020.15 Published online by Cambridge University Press

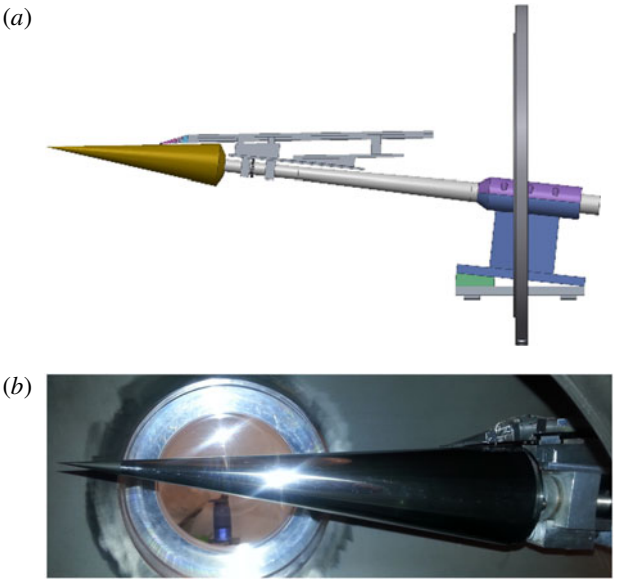


FIGURE 2. Schematic of cone model, sting and traversing mechanism and support base holding the model at a 6° angle of attack (*a*), and photograph of the cone model inside of the test section (*b*).

At the conditions of the experiment needed to produce a unit Reynolds number of 10×10^6 m^{-1}, the run time was approximately 80 ms. Further details of the facility are given by Cummings & McLaughlin (2012).

The inside diameter of the test section is 0.5 m, and its length is 0.98 m. For optical access, it has three 0.26 m flanged windows, two on opposite sides, and one on top. Measurements in the test section of the sister facility (Estorf *et al.* 2005) confirmed a non-uniformity of the Pitot pressure in the core flow of approximately $\pm 1.2\,\%$, corresponding to Mach number variations of $\pm 0.6\,\%$. This non-uniformity results from the narrow wake of the upstream fast-acting valve. To avoid this, the cone model was offset from the centreline of the test section.

The model is a hollow, thin-walled right-circular cone with a half-angle of $\phi_c = 7°$. The total length of the cone is 35.56 cm (14 in.). The first 4.303 cm (1.694 in.) (tip) of the cone is removable. The base of the cone mounted to a hollow sting that was connected to a vertical strut. The vertical strut bolted to a base plate that attached to the wind tunnel wall. An angled shim under the base plate was used to orient the cone at the $\alpha = 6°$ angle of attack. This gave an $\alpha/\phi_c = 0.86$, which was in the range of dimensionless angles where King (1992) had documented stationary cross-flow vortices.

A schematic of the cone, support sting and three-dimensional traversing mechanism that mounted on the support sting is shown in figure 2(*a*). A photograph of the cone in the wind tunnel test section is shown in figure 2(*b*). The wedge-shaped tip of the traversing mechanism that held a high bandwidth total-pressure probe is visible near the base of the cone. High-speed videos taken during a tunnel run confirmed minimal vibration of the traversing mechanism.

The traversing mechanism moved a total-pressure Pitot probe in the wall-normal, axial and azimuthal directions under computer control. Details of the traversing system

https://doi.org/10.1017/jfm.2020.15 Published online by Cambridge University Press

are given by Schuele (2011). The motion resolution in the axial direction was 0.1 mm. The resolution in the azimuthal direction was 0.035°, which was 228 times smaller than the most amplified stationary cross-flow mode azimuthal wavelength. An optical angle encoder provided feedback to the azimuthal positioning. The resolution in the wall-normal direction was 28 μm.

The total-pressure Pitot probe utilized Kulite model XCE-062-1.7A (1.7 bar, 25 psi absolute) pressure transducer that was mounted in the wedge tip of the traversing mechanism arm. The outside diameter of the Kulite transducer was 1.59 mm. The transducer was inserted into a circular sleeve whose inside diameter closely matched the outside diameter of the transducer body, and covered the diaphragm end of the pressure transducer. A series of three telescoping hypodermic tubes were then attached to the diaphragm end of the cylindrical sleeve, giving a final inside diameter of 0.43 mm, which was then the sensing diameter of the Pitot probe. This corresponded to 20 % of the most amplified stationary cross-flow mode azimuthal wavelength at the middle of the axial location (12.7 cm) where measurements were conducted. The total length of the hypodermic tube assembly was 12.5 mm, which was the same as that used by Schuele *et al.* (2013).

The frequency response of the Pitot probe, determined in the previous work (Corke *et al.* 2018), was 50 kHz. This was sufficient to capture the travelling cross-flow modes whose band of most amplified frequencies was centred near 35 kHz. The voltage time series from the pressure transducers were over-sampled at 2 MHz. These were later decimated in post-processing to a 100 kHz sampling frequency. This utilized a custom designed finite-impulse-response low-pass filter to prevent aliasing.

In the previous work, both 'critical' and 'subcritical' wavenumber discrete roughness tips were used. In the present experiment, only the 'critical' roughness wavenumber, $m = 45$, was investigated. Recall that this corresponds to the middle of the band of wavenumbers of the most amplified stationary cross-flow modes (Li *et al.* 2010). The receptivity of the stationary cross-flow mode to the 'critical' wavenumber roughness tip had been verified in the previous work (Corke *et al.* 2018).

As in the previous work, the axial location of the discrete roughness is based on linear stability analysis of Li *et al.* (2010) for the basic flow for the cone at the experiment conditions of angle of attack and unit Reynolds number. This information is compiled in figure 3. This shows the Branch I ($N = 0$) linear stability neutral curve for stationary cross-flow modes, as well as well as theoretical vortex lines along which the disturbances generated by the roughness convects. The roughness array was then located $x_r = 1.27$ cm from the tip of the cone. This is indicated by the vertical dashed line labelled x_r. Although the roughness encircles the whole tip, based on the vortex lines, only the roughness that falls in the range of approximately 30°–80° impacts the region where turbulent transition is most likely to occur based on linear stability N factors. For reference, the transition $N = 10$ curve is drawn on the figure. Previous experiments of cross-flow dominated transition at two different Mach numbers for this cone (Schuele *et al.* 2013; Corke *et al.* 2018) have found $N = 10$ to predict the transition location well.

The dashed box in the plot marks the region where boundary layer measurements were obtained. This corresponds to $130° \leqslant \theta \leqslant 140°$, and streamwise locations that bracket the transition $N = 10$ curve. The azimuthal extent of the measurements fully encompasses the 8° azimuthal wavelength of the $m = 45$ roughness.

https://doi.org/10.1017/jfm.2020.15 Published online by Cambridge University Press

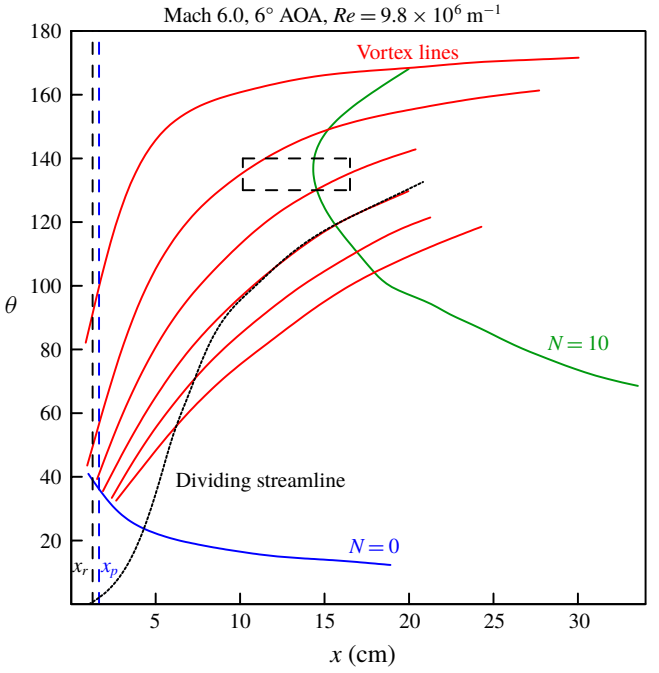


FIGURE 3. Linear stability and vortex path map used in determining axial location of discrete roughness for cross-flow transition control based on Li *et al.* (2010).

2.1. *Controlled unsteady disturbance generator*

The approach to introduce controlled unsteady disturbances in the boundary layer was based on the previous design by Schuele *et al.* (2013). In their case, a plasma actuator was designed to produce stationary cross-flow modes similar to the passive roughness. The approach was successful, demonstrating amplitude control of the stationary cross-flow modes for both 'critical' and 'subcritical' wavenumbers. In the present case, we sought to introduce controlled unsteady disturbances at a frequency that would be in the most amplified band of travelling cross-flow modes. The stationary cross-flow modes would be excited in the same manner as before, utilizing an azimuthal array of dimples located just upstream of the lower instability branch. However, in the present case, only the 'critical' ($m = 45$) azimuthal wavenumber roughness was investigated. Figure 4 shows photographs of the unassembled and assembled components of the cone tip that combines a roughness dimple array to excite stationary cross-flow modes at the 'critical' wavenumber ($m = 45$), and a plasma actuator ring to introduce an unsteady disturbance at a specific frequency.

The plasma actuator requires two electrodes separated by a dielectric material. The dielectric material in this case is Macor, a machinable ceramic. The Macor forms the middle section of the conical tip. The internal electrode consists of a cylindrical brass segment that is located inside a bored out hole in the centre of the Macor section. A wire lead that passes through the centre of the cone tip provides the AC electric connection to the internal electrode. The external electrode was formed by plating copper onto the surface of the Macor portion of the cone tip. The copper plating was vapour deposited to a thickness of 90 nm. The root-mean-square (r.m.s.) surface

https://doi.org/10.1017/jfm.2020.15 Published online by Cambridge University Press

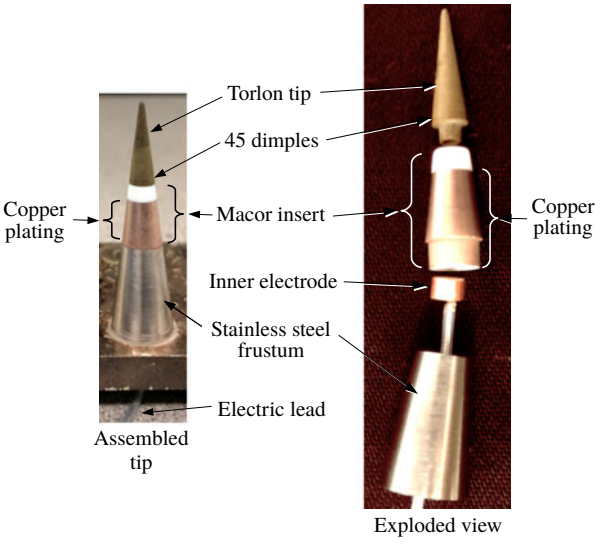


FIGURE 4. Photographs of exploded assembly view and fully assembled view of cone tip that combines dimples for stationary mode forcing and a plasma ring for travelling mode forcing.

roughness variation of the copper plating was verified to be well below that of the roughness dimples.

The copper plating wrapped completely around the Macor portion of the tip. It extended from approximately 3.5 mm downstream of the roughness dimples (1.65 cm from the cone tip) to the base of the Macor portion of the cone tip where, on assembly, it contacted a stainless-steel base. This contact to the stainless-steel provided an electrical connection to the metal cone model, which was earth grounded. This provided a current path to ground for the plasma actuator. The upstream location of the copper plating is denoted by the blue vertical dashed line with the notation x_p in figure 3.

The hardness of the Macor made it impossible to apply the roughness 'dimples' into its surface. Therefore, the leading portion of the cone tip was made from Torlon 5530, which is the same material previously used for the roughness tips (Corke *et al.* 2018). The Torlon tip mounted to the leading part of the Macor portion of the tip. The joints between the three components that made up the removable tip were successively polished with eight different grit-sized compounds starting from 1500 and ending at 8000. This was intended to provide smooth surfaces across the joints without steps or roughness. This was verified under a microscope. The fully assembled tip is shown in figure 4(*a*).

Figure 5 shows the roughness/plasma actuator cone tip operating in the Air Force Academy Mach 6.0 Ludwig tube during a data run. The plasma actuator frequency was 35 kHz, which is in the centre of the most amplified band based on linear theory (Li *et al.* 2010). This was also verified in the previous experiment results (Corke *et al.* 2018). The plasma (ionized air) appears as a purple ring around the cone tip. The left photo shows the plasma under ambient light. The right photo shows the plasma in the darkened laboratory.

The plasma actuator was started before initiating the tunnel run. In the Air Force Ludwieg tube operation, this was with the test section at the vacuum pressure.

https://doi.org/10.1017/jfm.2020.15 Published online by Cambridge University Press

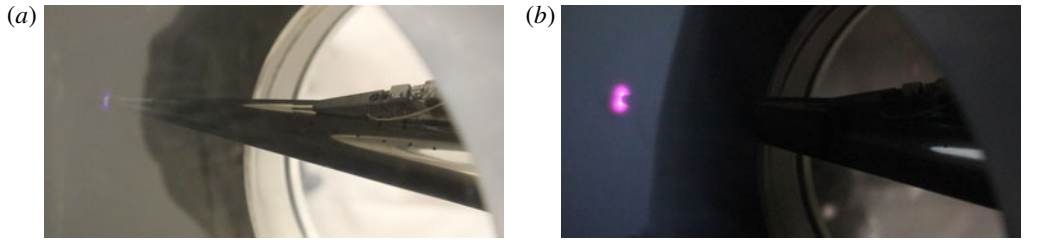


FIGURE 5. Photographs of cone tip with plasma actuator operating in the Mach 6.0 flow. Left view is with ambient light and right view is with the laboratory darkened.

Mach no.	6.0
T_0 (K)	480
P_0 (bar)	11.5
Unit Reynolds number (m^{-1})	10×10^6
Typical run time (ms)	80
Re_{x_r}	0.127×10^6
Roughness mode no.	45
Plasma actuator frequency (kHz)	35
Axial location (cm)	$10.2 \leqslant x \leqslant 16.5$
Azimuthal location (deg.)	$130 \leqslant \theta \leqslant 140$
Wall-normal location	$\sim y@p'_{max}$

TABLE 1. Summary of experimental conditions and measurement locations.

The plasma actuator was left on throughout the run, and then turned off after the completion of the run. The AC peak-to-peak voltage was kept constant. The majority of the data used a plasma actuator AC voltage of 5 kV. A few of the initial data runs utilized an AC voltage of 2.8 kV. These lower voltage cases were used to validate the receptivity of the travelling modes to the unsteady excitation. Measurements of the pressure transducer voltage time series with the plasma actuator operating without tunnel flow verified that there was no electronic noise component due to the plasma actuator.

The experiments were conducted with the same conditions as the previous (Corke *et al.* 2018) tunnel entries. These are listed in table 1. The measurements consisted of total-pressure time series taken at a fixed height above the surface of the cone. The height was determined to be where the total-pressure fluctuations were a maximum. This corresponded to a distance of 0.38 mm (0.015 in.) above the cone surface. The azimuthal extent was $130° \leqslant \theta \leqslant 140°$ in increments of 1°, and an axial extent of 10.16 cm $\leqslant x \leqslant$ 16.51 cm (4.0–6.5 in.) in increments of 1.27 cm (0.5 in.).

3. Results

Evidence that the boundary layer was receptive to the plasma actuator 35 kHz excitation is presented in figure 6. This shows a comparison of the frequency spectra of the total-pressure fluctuations with the plasma actuator excitation off and on at two voltage levels at the most downstream position, $x = 6.5$ in. (16.51 cm) and $\theta = 135°$. The ordinate of the spectrum plot is r.m.s. pressure fluctuations that have been normalized by the maximum r.m.s. level in the baseline (plasma off) condition. The

https://doi.org/10.1017/jfm.2020.15 Published online by Cambridge University Press

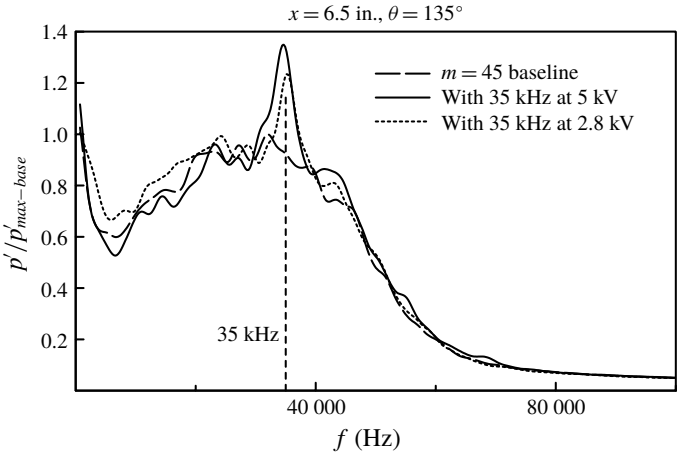


FIGURE 6. Spectra of pressure fluctuations normalized by the maximum baseline p' at $x = 6.5$ in. (16.51 cm) with plasma excitation off and on at 35 kHz with $V_{AC} = 5.0$ kV and 2.8 kV.

long dashed curve corresponds to the spectrum for the baseline case. The solid and short-dashed curves corresponds to the spectra with the plasma actuator operating at 35 kHz at AC peak-to-peak voltages of 5 kV and 2.8 kV, respectively. The baseline spectrum shows a broad peak centred around 30–35 kHz which is the expected most amplified band of frequencies of the travelling cross-flow modes (Li *et al.* 2010). With the plasma actuator operating, the spectra show a distinct peak at the 35 kHz excitation frequency. This is marked by the vertical dashed line at 35 kHz. The amplitude of the peak at 35 kHz increased with increasing AC voltage to the plasma actuator, further indicating the boundary layer response to the excitation.

Although the periodic excitation was designed to be at a single narrow-band frequency, the spectra of the total-pressure fluctuations in the boundary layer revealed a multitude of spectral peaks. As will be presented later, the streamwise location of the spectra in figure 6 corresponds to where the boundary layer is at a later stage of transition. Therefore, the presumption is that the distributed spectral peaks are the result of nonlinear interactions with the primary 35 kHz excitation. As a check, cross-bicoherence analysis was performed. The cross-bicoherence is a measure of the phase locking between two frequencies in two time series, with a third frequency in one of the two time series. The cross-bicoherence (CBC) is defined as

$$\beta_{ijk}(f_1, f_2) = \frac{|\tilde{R}_{ijk}(f_1, f_2)|^2}{\langle|\tilde{p}_i(f_1)|^2|\tilde{p}_j(f_2)|^2\rangle\langle|\tilde{p}_k(f_3)|^2\rangle}, \tag{3.1}$$

where

$$\tilde{R}_{ijk}(f_1, f_2) = \langle\tilde{p}_i(f_1)\tilde{p}_j(f_2)\tilde{p}_k^*(f_3)\rangle \tag{3.2}$$

is the cross-bispectrum, with i, j and k equal to either i or j that refer to one of the two mean-removed pressure time series, p, with frequencies f_1, f_2 and f_3, respectively. The notation ($\|$) is the modulus of the component, $\sim$ denotes the Fourier transformed function in the frequency domain, $\langle\rangle$ represents the ensemble average. These frequencies are related to each other such that $f_1 + f_2 + f_3 = 0$.

https://doi.org/10.1017/jfm.2020.15 Published online by Cambridge University Press

The value of the CBC varies between 0 and 1. High values of the CBC indicate a high degree of triple phase locking

$$\theta_i(f_1) + \theta_j(f_2) = \theta_k(f_3) \tag{3.3}$$

from realization to realization. Here, $\theta_i(f_1)$ is the instantaneous circular phase angle of $\tilde{p}_i(f_1)$.

The region of validity of the CBC is set by the Nyquist criterion, where the sum of any two frequencies cannot exceed half the sampling rate. This region then takes the form of two isosceles triangles, one each for sum and difference interactions.

In the Ludwieg tube operation, time series were sampled at one spatial location for each tunnel run. In contrast to the stationary cross-flow modes over which the discrete roughness on the cone tip provides a correlating factor from one run to the next, there is no equivalent correlating factor for the travelling disturbances (travelling cross-flow modes). Therefore in terms of the nonlinear frequency analysis, only single time series at one spatial location and corresponding to a single tunnel run were used. Thus in terms of the previous CBC notation for a single time series, $i = j = k = 1$, and $\theta_1(f_1) + \theta_1(f_2) = \theta_1(f_3)$. This is more specifically called auto-bicoherence (ABC). The ABC for the pressure time series measured at the same location as the spectra shown in figure 6 with the 35 kHz excitation and $V_{AC} = 5.0$ kV, is shown in figure 7. The upper triangle corresponds to summing frequency interactions. The lower triangle refers to difference frequency interactions. The filled colour contours indicate the ABC level which is an indication of the degree of triple frequency phase locking. The frequency f_1 is read from the abscissa of the rectangle that is drawn around the two triangles. The frequency f_2 is read from the ordinate of the rectangle drawn around the triangles. The ordinate origin is the horizontal line that separates the upper triangle from the lower triangle. The spectrum from figure 6 is displayed along the abscissa and ordinate. For the ordinate, the spectra are oriented so that zero frequency (DC) is aligned with the horizontal line separating the two triangles. Thus for the upper triangle with summing interactions, frequency increases from bottom to top, whereas for the lower triangle with difference interactions, frequency increases from top to bottom. The third frequency, f_3, in sum and difference interactions is read along the abscissa. This is found as a projection of a 45° diagonal from a point of intersection of f_1 and f_2 that intercepts the horizontal line that separates the upper and lower triangles. Examples of these have been drawn as blue arrows, with their projection to the abscissa shown as dotted arrows.

The 35 kHz excitation frequency on the abscissa and ordinate are indicated by the heavier red lines. Specific interactions occurring at the largest ABC levels are highlighted. For example, the summing interaction of the 35 kHz frequency has a high ABC indicating the triple phase locking $\theta(35\text{ kHz}) + \theta(35\text{ kHz}) = \theta(70\text{ kHz})$. The ABC, and CBC in general, only indicates phase locking. It does not indicate amplitude. The amplitude resulting from this interaction is determined from the auto-spectrum, which indicates only a small peak at approximately 70 kHz, and therefore does not contain much energy.

Following the example of the 70 kHz harmonic interaction, other interactions involving the primary 35 kHz input that are associated with other more major peaks in the spectrum have been highlighted. These were selected to merely demonstrate that a nonlinear phase locking existed between these frequencies and the primary input frequency that suggests their origin, and explains the appearance of the spectrum at a late stage of transition.

https://doi.org/10.1017/jfm.2020.15 Published online by Cambridge University Press

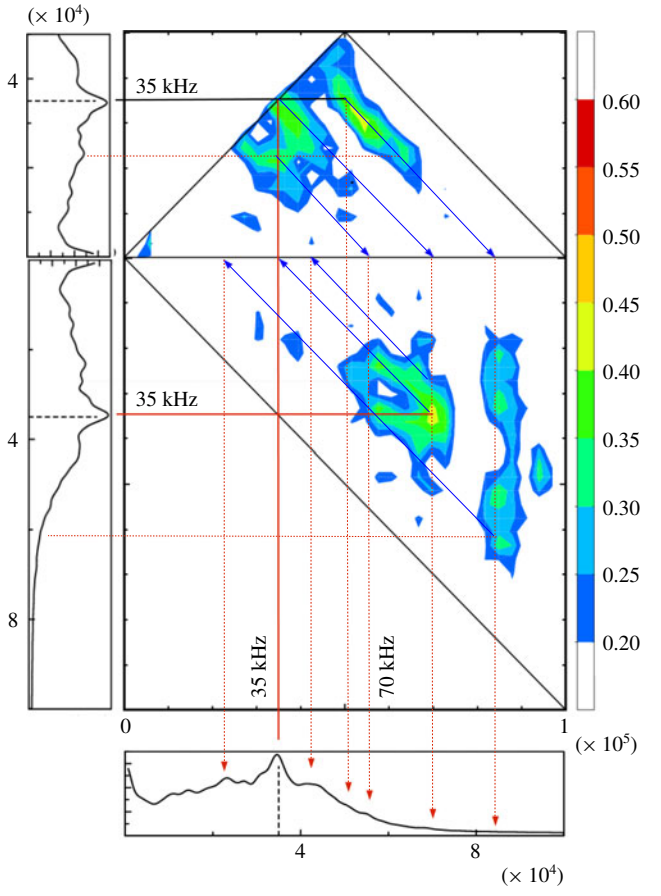


FIGURE 7. Auto-bicoherence of pressure time series measured at $x = 6.5$ in. (16.51 cm) with plasma excitation on at 35 kHz with $V_{AC} = 5.0$ kV. Shown along the axes are auto-spectra at the same conditions that were shown in figure 6.

The Pitot probe surveys were used to provide a direct measure of the mean flow distortion produced by the stationary cross-flow modes. This involved averaging the total-pressure time series taken over the duration of a run at each (θ, x) location.

Figure 8(*a*) shows the azimuthal variation in the time-average total pressure at a fixed height above the cone surface with the $m = 45$ roughness tip. The effect of the azimuthal variation in the average total pressure due to the azimuthally thickening boundary layer has been removed. The colour rendering of the total pressure is then presented as the deviation (plus or minus) about the local mean value. This clearly reveals the azimuthal variation in the total pressure that is indicative of the mean flow distortion produced by the stationary cross-flow mode. Note that negative mean-removed pressures correspond to a locally thickened portion of the boundary layer, and positive mean-removed pressures correspond to locally thinned portions. The dotted curve in the figure traces out the x-development of an azimuthally thickened portion of the boundary layer. This trajectory should correspond to that of two neighbour stationary cross-flow vortices. This was confirmed in our previous work

https://doi.org/10.1017/jfm.2020.15 Published online by Cambridge University Press

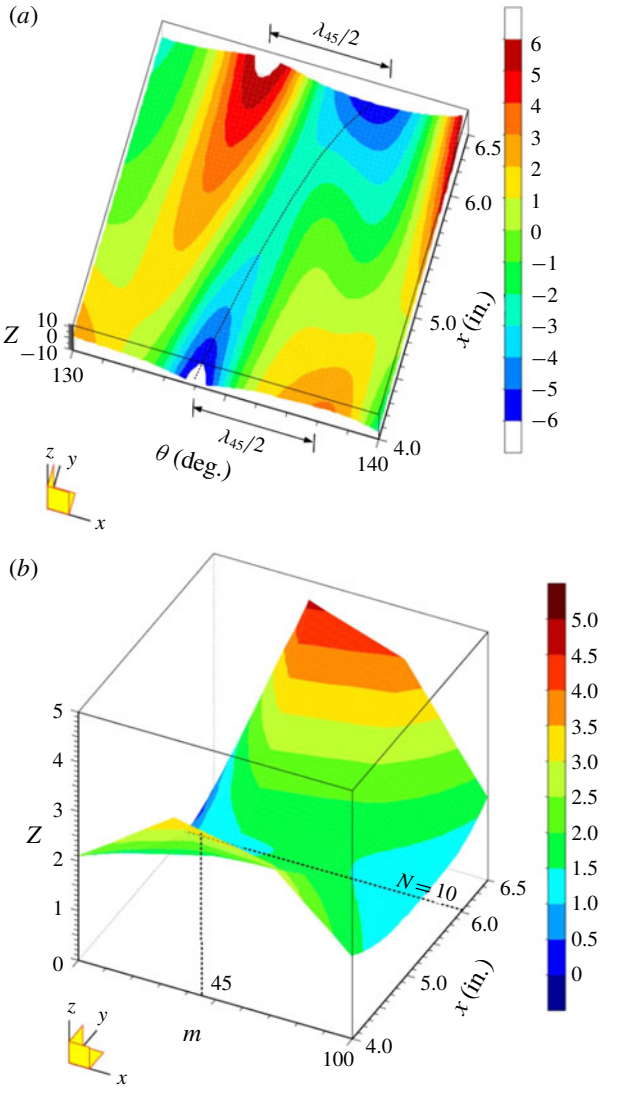


FIGURE 8. Azimuthal total-pressure distributions at a constant height above the surface (*a*) and corresponding wavenumber spectra (*b*) for the case with the 'critical' ($m = 45$) roughness cone tip without plasma excitation.

(Corke *et al.* 2018), where similar traces were found to perfectly overlay stationary patterns in surface flow visualization images.

The stationary cross-flow mode that corresponds to the $m = 45$ roughness has an azimuthal wavelength of 8°, namely 360°/45. Its half-wavelength then corresponds to $\theta = 4°$, which has been denoted in figure 8(*a*) as $\lambda_{45}/2$. This appears to closely correspond to the spacing between the peak and valley in the azimuthal pressure distribution, and therefore is a good indication that the mean flow distortion is the result of the growth of the prescribed stationary cross-flow mode. This is further illustrated by the azimuthal wavenumber spectra of this total-pressure distribution that is presented in figure 8(*b*). This shows a predominant peak centred about $m = 45$.

https://doi.org/10.1017/jfm.2020.15 Published online by Cambridge University Press

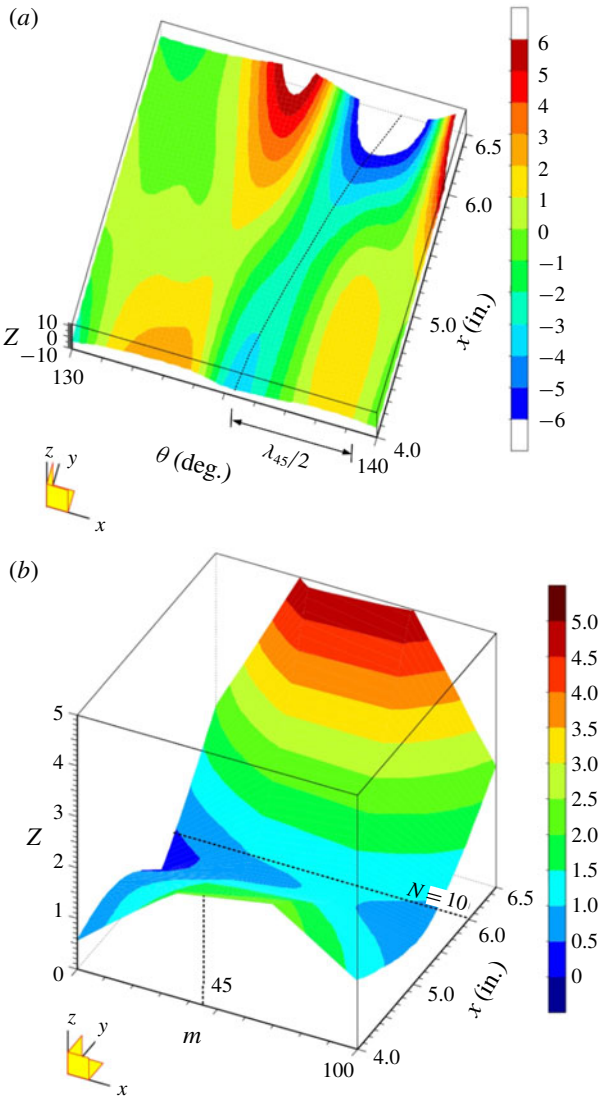


FIGURE 9. Azimuthal total-pressure distributions at a constant height above the surface (*a*) and corresponding wavenumber spectra (*b*) for the case with the 'critical' ($m = 45$) roughness cone tip with 35 kHz, 5.0 kV plasma excitation.

The energy about $m = 45$ decays to a minimum near the axial location where the $N = 10$ factor, denoted in the figure, would predict where transition would occur. This agrees well with our previous work (Corke *et al.* 2018) based on similar mean total-pressure surveys and surface flow visualization.

The effect of the 35 kHz excitation on the spatial development of the mean flow distortion produced by the $m = 45$ roughness tip is shown in figure 9. Figure 9(*a*) documents the mean flow distortion. Comparing this to that in figure 8(*a*) without 35 kHz excitation, indicates some differences. In particular, at the upstream location, the azimuthal variation in the total pressure is smaller, indicating a more uniform boundary layer thickness with less mean distortion. As a reference, $\lambda_{45}/2$ is again

https://doi.org/10.1017/jfm.2020.15 Published online by Cambridge University Press

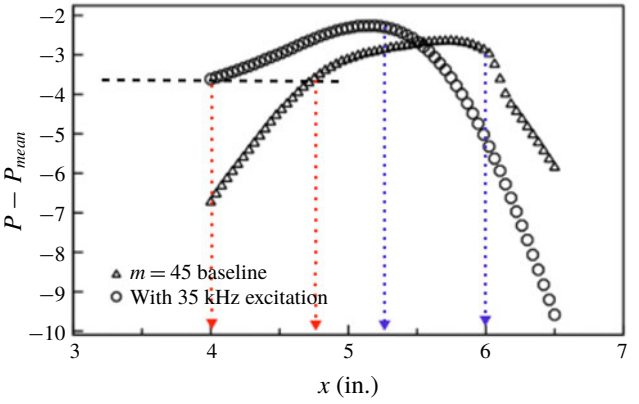


FIGURE 10. Axial distributions following the pressure minima denoted by the dotted curve in the total-pressure distributions in figures 8(*a*) and 9(*a*).

indicated in the figure. We note that the wavelength match to $m = 45$ is not as precise as that without the 35 kHz excitation, although that could be the result of the having a weaker mean flow distortion.

The azimuthal wavenumber spectra of the total-pressure distribution for the $m = 45$ tip with the 35 kHz excitation is shown in figure 9(*b*). This indicates that $m = 45$ is in the band of prominent wavenumbers. However in contrast to the previous case without the 35 kHz excitation, the energy in the $m = 45$ mode decays to a minimum well upstream of the $N = 10$ factor axial location. Thus this indicates that turbulent transition occurred earlier with the addition of the periodic excitation.

As further evidence of the effect of the 35 kHz excitation on the transition location, the method of Schuele *et al.* (2013) was used to estimate the transition location. This involved following the (x, θ)-trajectory of a minimum in the total pressure distributions in figures 8(*a*) and 9(*a*). The actual trajectories are shown by the dotted curves in those two figures. As previously mentioned, the pressure minima are indicative of a region of local thickening of the boundary layer. Such regions are known to develop an off-wall inflectional shear layer and subsequent inviscid instability that quickly leads to turbulence (Saric *et al.* 2003; Craig & Saric 2016). The ending azimuthal locations of both of these trajectories ($138° \leqslant \theta \leqslant 140°$) is where the transition $N = 10$ curve is furthest upstream on the cone and therefore where transition is expected to occur first.

The x-development of the total pressure along the two pressure minima for the $m = 45$ roughness with the 35 kHz excitation off and on is shown in figure 10. At a fixed height above the surface, the streamwise development of the local total pressure is an indication of the wall shear stress (Preston 1954). The onset of transition is normally observed as a rise in the shear stress (total pressure) above a common reference. A reference that can apply to the two cases is shown by the horizontal dashed line. The x-locations of the intersection of the reference line with the total-pressure distribution represents the respective transition locations. These are shown by the red dotted vertical lines. This indicates that the onset of transition moved upstream by approximately 16 % with the addition of the 35 kHz excitation.

An indication of the last stage of turbulent transition is evident in a rapid reduction of the total pressure, signifying a rapid thickening of the boundary layer. The blue dotted vertical lines provide estimates of the beginning of that process for the two

https://doi.org/10.1017/jfm.2020.15 Published online by Cambridge University Press

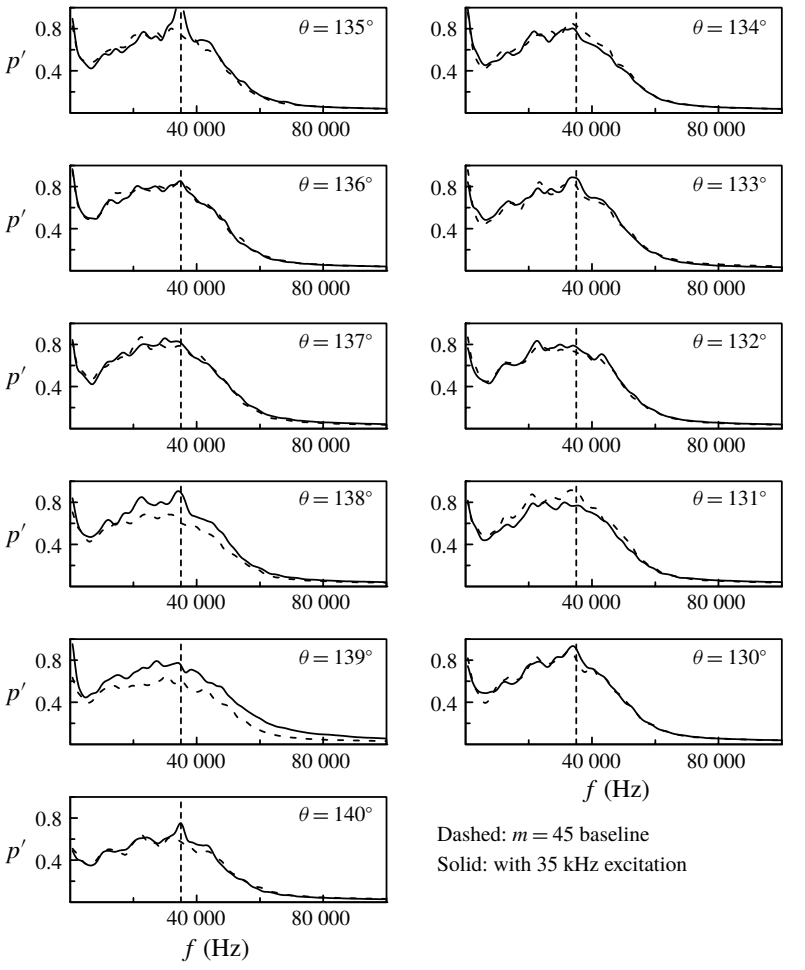


FIGURE 11. Sample comparison of spectra of travelling disturbances at different azimuthal positions at $x = 16.51$ cm (6.5 in.) with $m = 45$ roughness without and with plasma excitation at 35 kHz and 5 kV_{AC}.

cases. For the baseline case with the 35 kHz excitation off, the transition location is estimated to be at $x = 6.0$ in. (15.24 cm), which is very close to the transition $N = 10$ line that was shown in figure 3. This was also close to the transition location with the $m = 45$ 'critical' roughness case in our previous experiment (Corke *et al.* 2018). Based on the last stage transition, the addition of the 35 kHz excitation caused its location to move upstream by approximately 12.5 %.

As previously mentioned, the total-pressure Pitot probe had a frequency response that was capable of detecting the travelling cross-flow modes. One representation of spectra of total-pressure fluctuations at one azimuthal location in the boundary layer for $x = 16.51$ cm (6.5 in.) was shown in figure 6. Figure 11 shows spectra of the off-wall pressure fluctuations for all of the azimuthal locations at $x = 16.51$ cm (6.5 in.) with the $m = 45$ roughness tip and the 35 kHz excitation off and on. As in figure 6, the dashed curve corresponds to the baseline spectra with the plasma actuator off, and the solid curve corresponds to the spectra with the plasma actuator operating at

https://doi.org/10.1017/jfm.2020.15 Published online by Cambridge University Press

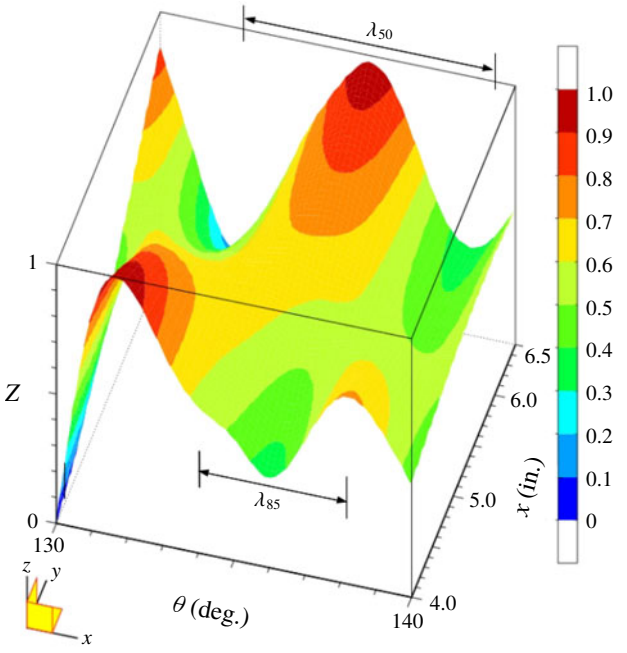


FIGURE 12. Spatial amplitude distribution of the spectral peak amplitude of the travelling disturbances for the $m = 45$ roughness tip without 35 kHz, 5 kV_{AC} excitation.

35 kHz and 5 kV_{AC}. The vertical dashed line indicates the 35 kHz frequency in the spectra. These spectra indicate that there is an azimuthal variation to the effect of the 35 kHz excitation on the baseline spectra. A similar variation occurred at all of the axial locations.

To investigate the azimuthal variation in the effect of the 35 kHz excitation, the peak values of the spectra of the travelling disturbances from spectra like those in figure 11 for all of the measured (θ, x) locations, were used to compile a view of the spatial amplitude distribution for the travelling cross-flow modes. These are shown for the $m = 45$ roughness cone tip without the 35 kHz excitation in figure 12, and for the same roughness tip with the 35 kHz, 5 kV_{AC} excitation in figure 13. Examination of these reveals the presence of features with different azimuthal wavenumbers. As before, to interpret these, one needs to consider possible interactions between the travelling and stationary cross-flow modes.

The underlying assumption of the 35 kHz excitation is that it would impart energy into the band of most amplified travelling cross-flow modes. As observed in the previous results (Corke *et al.* 2018), a nonlinear (quadratic) summing interaction between travelling and stationary cross-flow modes led to observable spatial amplitude distributions in the temporal (travelling) disturbances that could be associated with travelling cross-flow modes.

Utilizing the $m = 45$ roughness tip, figure 8 documents stationary modes with that azimuthal wavenumber. This mode is designated $(0, 45)$, where the first index is the frequency, and the second is the azimuthal wavenumber. Based on Li *et al.* (2010), the most amplified travelling cross-flow mode occurs with an azimuthal wavenumber of $m = 40$. The travelling mode is then designated as $(f_t, 40)$, where f_t refers to the frequency of the travelling mode.

https://doi.org/10.1017/jfm.2020.15 Published online by Cambridge University Press

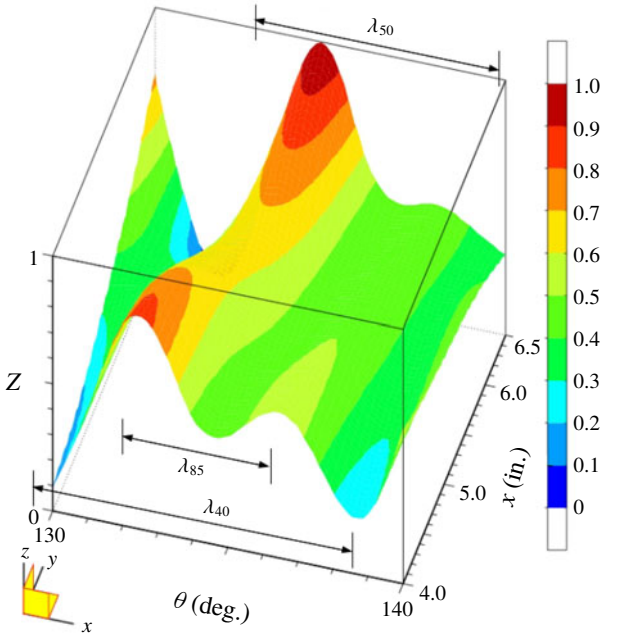


FIGURE 13. Spatial amplitude distribution of the spectral peak amplitude of the travelling disturbances for the $m = 45$ roughness tip with 35 kHz, 5 kV_{AC} excitation.

The first interaction between these two modes is

$$(0, 45) \pm (f_t, 40) = (f_t, 85) \quad \text{and} \quad (f_t, 5), \tag{3.4}$$

where $(f_t, 85)$ and $(f_t, 5)$ are travelling modes with the same frequency as the primary travelling mode. Therefore, the amplitude of the spectral peaks in figure 11 should be representative of not only the primary travelling mode, but also the sum and difference modes that occur at the same frequency.

Now, the result of the summing interaction, $(f_t, 85)$, would have an azimuthal wavelength of approximately 4°. That of the difference interaction, $(f_t, 5)$, would have an azimuthal wavelength of 72°. The latter is larger than the azimuthal extent of the measurements. However the former, $(f_t, 85)$, is slightly distinguishable in the spatial amplitude distribution in figure 12 by the small bump at $\theta = 134°$ at the most upstream x-position.

Also observable is a spatial amplitude distribution with an azimuthal wavenumber corresponding to $m = 50$ with an azimuthal wavelength designated as λ_{50}. An explanation for this will come from cross-bicoherence results to follow.

For the case with the $m = 45$ roughness tip and the 35 kHz excitation, the spatial distribution of travelling disturbances is quantitatively different. In particular, there is a strong appearance of the summed mode, $(f_t, 85)$, with azimuthal wavelength, λ_{85}, and the amplitude variation with the azimuthal wavelength of λ_{50}. The stronger presence of the former is a good indication that the 35 kHz excitation was indeed imparting energy into the most amplified travelling cross-flow mode with an azimuthal wavenumber, $m = 40$.

In order to further contrast the differences in the travelling mode spatial amplitude distributions with the 35 kHz excitation, the azimuthal wavenumber spectra of the

https://doi.org/10.1017/jfm.2020.15 Published online by Cambridge University Press

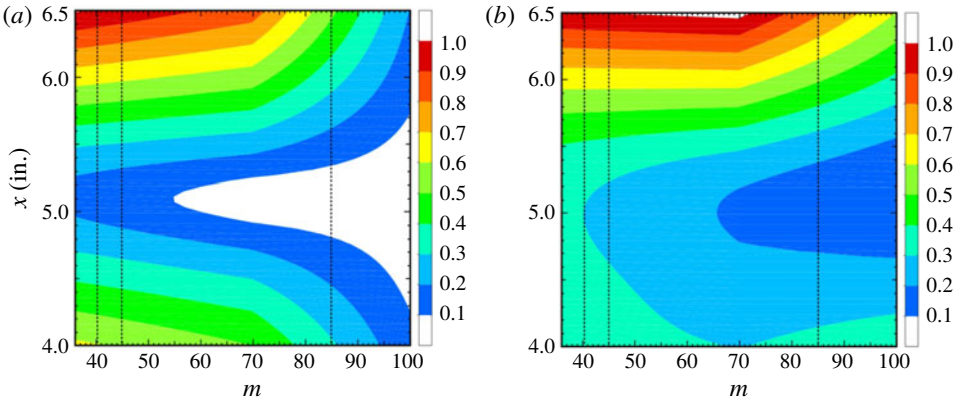


FIGURE 14. Axial development of the azimuthal wavenumber of the maximum pressure fluctuations of $m = 45$ roughness tip based on figure 12 with the plasma excitation at 35 kHz off (a) and based on figure 13 with the plasma excitation at 35 kHz and 5 kV_{AC} on (b).

distributions in figures 12 and 13 were computed and these are presented in figure 14. Figures 14(a) and 14(b), respectively, correspond to the cases without and with the 35 kHz excitation. The most notable difference between these two is the energy at wavenumbers centred about $m = 85$ that occurs with the 35 kHz excitation and that is absent without the excitation.

As was previously done (Corke *et al.* 2018), the cross-bicoherence statistic was used to document the nonlinear interaction between stationary and travelling cross-flow modes. Because it involves the stationary cross-flow mode with a known wavenumber, the CBC is now defined in terms of wavenumber, m, namely

$$\beta_{ijk}(m_1, m_2) = \frac{|\tilde{R}_{ijk}(m_1, m_2)|^2}{\langle|\tilde{p}_i(m_1)|^2|\tilde{p}_j(m_2)|^2\rangle\langle|\tilde{p}_k(m_3)|^2\rangle}, \tag{3.5}$$

where

$$\tilde{R}_{ijk}(m_1, m_2) = \langle\tilde{p}_i(m_1)\tilde{p}_j(m_2)\tilde{p}_k^*(m_3)\rangle \tag{3.6}$$

is the cross-bispectrum. These wavenumbers are related to each other such that $m_1 + m_2 + m_3 = 0$.

Following the previously approach used by Corke *et al.* (2018), one of the data series in the CBC is the azimuthal variation in the time-averaged total pressure, $\bar{p}(\theta)$, at a selected x location on the cone. The same data were used to generate figures 8(a) and 9(a). This data series therefore represents the azimuthal mean flow distortion at one x location. The Fourier transform of this data series is $\tilde{\bar{p}}(m)$. The wavenumber spectra shown in figures 8(b) and 9(b) correspond to $|\tilde{\bar{p}}(m)|^2$ at each x location.

The second data series used in the CBC corresponds to the total pressure time series before time averaging, $p(t)(\theta)$, at the same x location as $\bar{p}(\theta)$. This data series contains pressure fluctuations that correspond to the travelling cross-flow modes. The squared modulus of the transformed data series, $|\tilde{p}(f)|^2$, was used to generate the frequency spectra that were shown in figure 11.

It is necessary that the two transformed data series have the same independent variable units. In $|\tilde{p}(m)|^2$, the independent variable is azimuthal wavenumber, m. In

https://doi.org/10.1017/jfm.2020.15 Published online by Cambridge University Press

$|\tilde{p}(f)|^2$ the independent variable is frequency, f. Therefore, in the case of the latter, we chose to convert frequency to azimuthal wavenumber. As previously pointed out, the analysis by Li *et al.* (2010) indicated that the azimuthal wavenumber in the centre of the most amplified band of frequencies of the travelling cross-flow mode (35 kHz) was $m = 40$. This was used as a point of reference for the conversion from frequency to wavenumber of the travelling mode data series.

Another important step in computing the CBC was that the sampling rates be the same for the two data series. For the time series representing the stationary cross-flow mode, $\bar{p}(\theta)$ (data series 1), the sampling rate was 8.54 pts/$\circ$. For the time series representing the travelling cross-flow mode (data series 2), the sampling rate was considerably less at 0.317 pts $\circ^{-1}$. Therefore, in order to match the two data sampling rates, data series 2 was zero padded by the appropriate amount prior to the Fourier transform.

Again, the value of the CBC varies between 0 and 1. High values of the CBC indicate a high degree of triple phase locking, which in terms of wavenumbers is

$$\theta_i(m_1) + \theta_j(m_2) = \theta_k(m_3), \tag{3.7}$$

from realization to realization. Here $\theta_i(m_1)$ is the instantaneous circular phase angle of $\tilde{p}_i(m_1)$.

As a reminder, the region of validity of the CBC is set by the Nyquist criterion, where the sum of any two frequencies (or wavenumbers in this case) cannot exceed half the sampling rate. This region again takes the form of two isosceles triangles, one each for sum and difference interactions.

For the CBC, the data series corresponding to the stationary cross-flow modes was designated data series 1 (subscript 1 in (3.5)). The data series corresponding to the travelling cross-flow modes was designated data series 2 (subscript 2, in (3.5)).

Starting with the two data series, there are 2^3 combinations of i, j and k in the calculation of $\beta_{ijk}(m_1, m_2)$ in (3.5). Based on the results in figures 12–14, that indicate an influence of the stationary cross-flow mode on the spatial amplitude distribution of the travelling cross-flow mode, we chose the order to be $[i, j, k] = [1, 2, 2]$. Thus, we were investigating an interaction between stationary modes (1) and the travelling modes (2) that results in travelling modes (2) at sum and difference wavenumbers.

A CBC result for the present experiment is shown in figure 15(*a*). This corresponds to $m = 45$ discrete roughness and 35 kHz, 5 kV_{AC} excitation measured at the most upstream location of $x = 10.16$ cm (4.0 in.), and $\theta = 135°$. This CBC is typical to all the azimuthal positions at this axial location. The wavenumber of the stationary modes, m_1, is read from the abscissa of the rectangle encompassing the CBC domain triangles. The wavenumbers of the travelling modes, m_2, are read from the ordinate of the rectangle. The ordinate wavenumbers are either added (top triangle) or subtracted (bottom triangle) from those read on the abscissa to give the third frequency, which is read as the intercept of a $-45°$ line to the abscissa.

Figure 15(*a*) shows two large wavenumber regions where the CBC indicates significant triple frequency phase locking. Interactions involving the $m = 45$ stationary mode and the $m = 40$ (35 kHz) travelling mode are highlighted by the arrows. One of these is a summing interaction

$$(0, 45) + (f_t, 40) = (f_t, 85). \tag{3.8}$$

The nearly perfect CBC for this interaction confirms it to be the source of the $m = 85$ spatial amplitude distribution of travelling disturbances that was documented in figure 13.

https://doi.org/10.1017/jfm.2020.15 Published online by Cambridge University Press

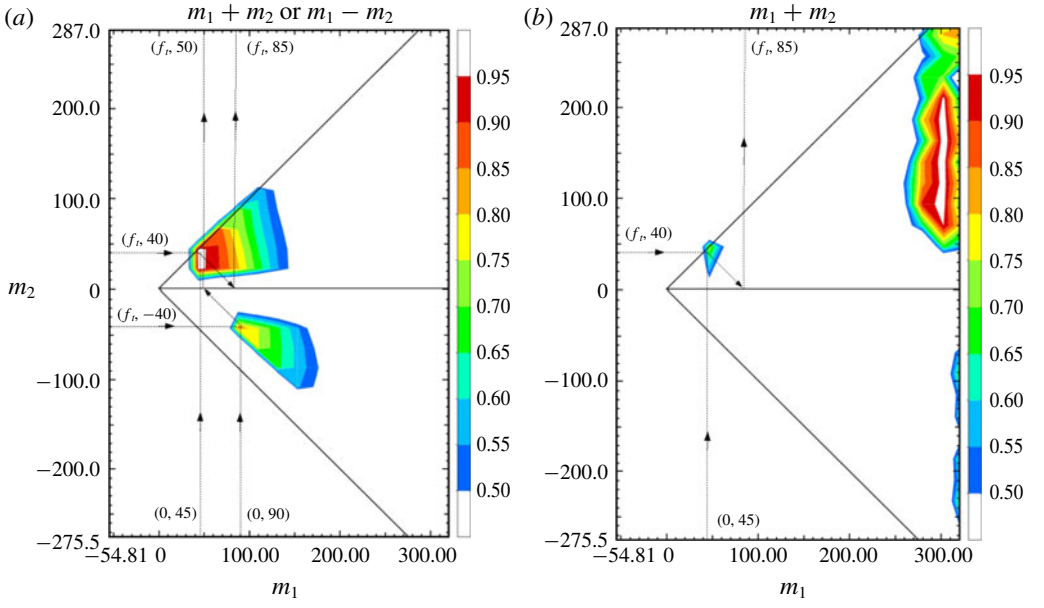


FIGURE 15. Cross-bicoherence for stationary–travelling–travelling mode interactions with $m = 45$ roughness tip and plasma excitation at 35 kHz and 5 kV_{AC} (*a*) and for comparison the previous result from Corke *et al.* (2018) with $m = 45$ roughness tip alone (*b*).

Another spatial amplitude distribution that was documented in figure 13 corresponded to $m = 50$. The CBC in figure 15(*a*) indicates that this results from a difference interaction involving a harmonic of the $m = 45$ stationary mode namely

$$(0, 90) - (f_t, 40) = (f_t, 50). \tag{3.9}$$

In order to contrast the present results with the 35 kHz excitation, the CBC from the previous experiments (Corke *et al.* 2018) is presented in figure 15(*b*). The conditions of the previous experiment were identical to those of the present experiment, with the only difference being the lack of the controlled unsteady disturbance input. That case also documented the summing interaction that could account for the $(f_t, 85)$ mode. However, the range of summing interaction wavenumbers was significantly smaller. Also noted in the previous CBC was the lack of difference interactions. Finally, the CBC in the previous experiment revealed strong triple phase locking in summing interactions between higher stationary wavenumbers and a broad range of wavenumbers of travelling modes. It was presumed that the higher stationary wavenumbers might represent uncontrolled surface roughness on the cone tip. These did not appear in the present experiment. However, as will be discussed, it points to a possible mechanism of spectral broadening at transition.

4. Discussion

As previously stated, the observations in our earlier experiment of the quadratic interaction between the stationary and most amplified traveling cross-flow modes (Corke *et al.* 2018), led to the speculation that effects on the traveling modes initial

https://doi.org/10.1017/jfm.2020.15 Published online by Cambridge University Press

amplitude, such as through free-stream disturbances, could impact transition, and transition control.

Neel *et al.* (2018) investigated the effect of free-stream disturbances on stationary cross-flow modes on elliptic cross-section cones at Mach 6.0. The disturbance levels were varied based on the position of the model within the nozzle expansion. The presence of stationary cross-flow modes was determined by thermal imaging, where they appeared as elevated temperature streaks. They observed that the lower disturbance level produced more distinct streaks compared to the higher disturbance condition.

Borg and colleagues (Borg, Kimmel & Stanfield 2011, 2012, 2013; Borg *et al.* 2015; Borg & Kimmel 2016) performed a series of experiments that focused on various elements of the transition process on a Hypersonic International Flight Research Experimentation (HIFiRE) program 2 : 1 elliptic cone which under 'quiet' flow conditions, exhibited travelling cross-flow waves. They particularly focused on the effect of free-stream disturbances. These experiments utilized surface mounted pressure transducers to measure pressure fluctuations within the transitional boundary layer. Spectra under 'quiet' flow revealed a peak that was centred near 45 kHz that was believed to be due to travelling cross-flow modes. The peak magnitude was seen to increase with increasing Reynolds number and then to broaden and fill all frequencies, indicating fully turbulent flow.

Using the same elliptic cone model, Borg *et al.* (2015) examined the effect of free-stream noise on transition under 'noisy' conditions in the Purdue Boeing/AFOSR Mach-6 Quiet Tunnel (BAM6QT) operated with the bleed valves closed, as well as in the conventional Texas A&M University Adaptively Controlled Expansion (TAMU ACE) hypersonic tunnel. The spectral content of the wall pressure fluctuations looked similar across the two facilities, suggesting a comparison could be made between bleed off and on in regard to the impact of free-stream disturbances on cross-flow transition. However, the exact cause of the transition under 'noisy' flow, or the effect of significantly varying noise levels, was not obtained.

In 'quiet' design supersonic and hypersonic wind tunnels, the level of disturbance is binary, produced by having the boundary bleed off ('noisy') or on ('quiet'). In addition, the disturbance amplitudes and spectrum under 'noisy' conditions are either unknown, or with a broad content. That was the motivation for introducing periodic disturbances of known and repeatable frequency and amplitude directly in the boundary layer.

As evidenced by figure 6, spectra of total pressure fluctuations in the boundary layer confirmed the receptivity of the boundary layer to the 35 kHz excitation. This included a response to the change in the amplitude of the excitation that was controlled through the AC voltage input. The 35 kHz frequency was chosen because it was in the centre band of the most amplified frequencies of the travelling cross-flow mode based on the linear theory analysis of Li *et al.* (2010). In addition, and importantly in terms of tracking mode interactions, the 35 kHz travelling cross-flow mode was predicted to have an azimuthal mode number of $m = 40$.

The off-wall azimuthal surveys of the total pressure revealed the same picture as our previous work (Corke *et al.* 2018), of the mean flow distortion produced by the stationary cross-flow modes, and again confirmed the receptivity of the stationary cross-flow mode to the discrete roughness in the conventional ('non-quiet' design) environment. In contrast to our previous work, only the 'critical' azimuthal wavenumber roughness, $m = 45$, was investigated. Thus our intention was to investigate the effect of the initial amplitude of the most amplified travelling cross-flow mode on transition of the most amplified band of stationary cross-flow modes.

https://doi.org/10.1017/jfm.2020.15 Published online by Cambridge University Press

Estimates of the transition location were based either on an increase in the total pressure near the cone surface, signifying an early transition stage, or a rapid thickening of the boundary layer, signified by a decrease in the total pressure near the cone surface that signified a late stage of transition. This was measured along the trajectory of the stationary cross-flow mode, where the boundary layer was thickest due to the mean flow distortion. For the baseline case with the 35 kHz excitation off, the transition location agreed well with the $N = 10$ prediction. This also agreed well with the previous experiment (Corke *et al.* 2018). With the 35 kHz excitation, the transition location moved upstream by approximately 9 %.

The underlying assumption of the 35 kHz excitation is that it would impart energy into the band of most amplified travelling cross-flow modes. This is supported by evidence of an interaction between the stationary and travelling cross-flow modes that was embodied in the spatial amplitude distribution of travelling disturbances that was shown in figure 13. Recall that this was the result of hundreds of individual wind tunnel runs, with the only constants, besides Reynolds number, being the controlled discrete roughness and 35 kHz excitation.

The spatial amplitude distribution showed evidence of a quadratic interaction between the linearly amplified travelling and stationary cross-flow modes. For the critical roughness with frequency and a mode number of (0, 45), this led to the generation of a travelling mode (f_t, 85) with the same frequency as the primary travelling mode, f_t. The spatial amplitude distribution also showed evidence of another travelling mode with an azimuthal wave angle of approximately 7° that would correspond to $m = 50$. As the CBC showed, the source of this $m = 50$ mode was not the result of a direct interaction between the $m = 45$ discrete roughness, but rather of the harmonic wavenumber of the roughness with $m = 90$. This resulted in a travelling mode with the same frequency as the primary travelling mode, namely (f_t, 50). Similar interactions with a broad spectrum of surface roughness wavenumbers that interact with the band of travelling cross-flow modes could present a mechanism that influences the transition location based on the level of free-stream disturbances. This is illustrated in figure 16, in which a broad range of stationary wavenumbers presumed to originate from random surface roughness, could interact with the broadly amplified band of travelling disturbance wavenumbers in a summing interaction that yields a very broad band of travelling disturbance wavenumbers. A similar process could emerge through difference interactions. This scenario would result in rapid spectral broadening that is associated with turbulent transition. It further points to a mechanism for the sensitivity of cross-flow transition to the level of free-stream disturbances that has been observed by others (Borg *et al.* 2011, 2012, 2013, 2015; Borg & Kimmel 2016).

5. Conclusions

Experiments were performed to further investigate a quadratic interaction between stationary and travelling cross-flow modes that were revealed in the previous experiment by Corke *et al.* (2018) on a sharp right-circular cone at an angle of attack at Mach 6.0. As before, passive discrete roughness was applied near the cone tip, just upstream of Branch I of the linear stability neutral curve for stationary cross-flow modes. The passive roughness consisted of indentations (dimples) that were evenly spaced azimuthally to excite a specific azimuthal wavenumber. The azimuthal wavenumber of the roughness was selected to be in the centre of the band of most amplified stationary cross-flow modes based on linear theory. A plasma actuator was

https://doi.org/10.1017/jfm.2020.15 Published online by Cambridge University Press

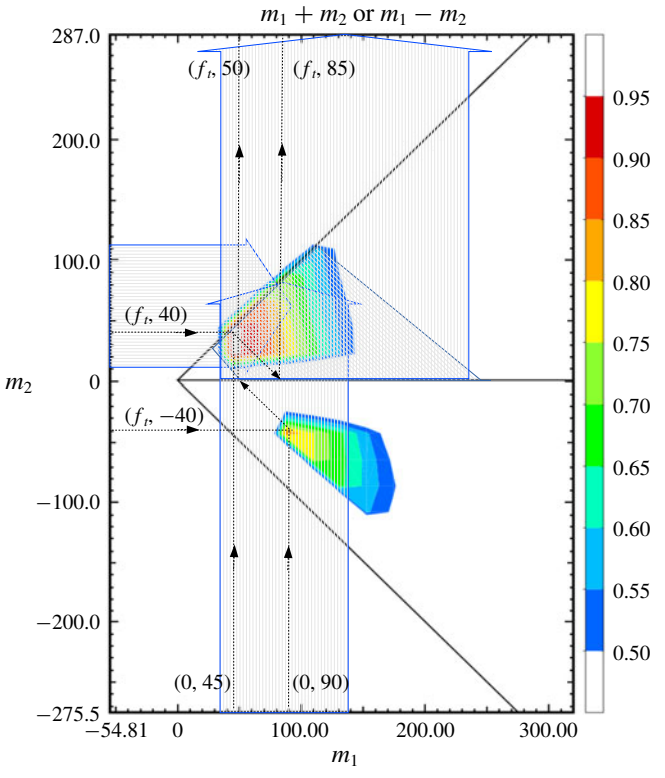


FIGURE 16. Example of cross-bicoherence for stationary–travelling–travelling mode interactions that could result in spectral broadening associated with transition to turbulence.

located just downstream of the discrete roughness array. This was designed to produce an azimuthally uniform unsteady disturbance with a frequency that was at the centre of the band of most amplified travelling cross-flow modes.

Time-averaged off-wall total-pressure measurements of the mean flow distortion confirmed that the stationary cross-flow mode was receptive to the passive discrete roughness. Spectra of total-pressure fluctuations verified the receptivity of the boundary layer to the unsteady excitation. The addition of the unsteady excitation was found to influence the azimuthal and streamwise development of the stationary and travelling cross-flow modes. The global effect was to move the transition location upstream by approximately 16 %.

The unsteady excitation was found to greatly enhance the quadratic interaction between stationary and travelling cross-flow modes that was first observed by Corke *et al.* (2018). This was made evident by a significantly enlarged band of wavenumbers over which sum and difference wavenumber interactions occurred. This suggests a scenario where a broad spectrum of free-stream disturbances of sufficient amplitude could interact with a broad spectrum of stationary disturbances produced by randomly distributed surface roughness that leads to rapid spectral broadening and turbulence.

In the present experiment, the unsteady excitation was introduced within the boundary layer. Assuming a sufficient receptivity to external disturbances, this still suggests a scenario for turbulent transition that is sensitive to the external flow environment. Quantifying such sensitivity is critical to transition prediction as well as

https://doi.org/10.1017/jfm.2020.15 Published online by Cambridge University Press

to methods of transition control that are equally critical to viscous drag and surface heating on hypersonic vehicles.

Acknowledgement

This work was supported by the Air Force Office of Scientific Research under grant FA9550-15-1-0278 that is monitored by Dr I. Leyva.

Declaration of interests

The authors report no conflict of interest.

REFERENCES

BIPPES, H. 1999 Basic experiments on transition in three-dimensional boundary layers dominated by crossflow instability. *Prog. Aerosp. Sci.* **35**, 363–412.

BONFIGLI, G. & KLOKER, M. 2007 Secondary instability of crossflow vortices: validation of the stability theory by direct numerical simulation. *J. Fluid Mech.* **583**, 229–272.

BORG, M. & KIMMEL, R. 2016 Simultaneous infrared and pressure measurements of crossflow instability modes for HIFiRE-5. In *54th AIAA Aerospace Sciences Meeting*. American Institute of Aeronautics and Astronautics.

BORG, M., KIMMEL, R., HOFFERTH, J., BOWERSOX, R. & MAI, C. 2015 Freestream effects on boundary layer disturbances for HIFiRE-5. In *53rd AIAA Aerospace Sciences Meeting*. American Institute of Aeronautics and Astronautics.

BORG, M., KIMMEL, R. & STANFIELD, S. 2011 HIFiRE-5 attachment-line and crossflow instability in a quiet hypersonic wind tunnel. In *41st AIAA Fluid Dynamics Conference and Exhibit*. American Institute of Aeronautics and Astronautics.

BORG, M., KIMMEL, R. & STANFIELD, S. 2012 Crossflow instability for HIFiRE-5 in a quiet hypersonic wind tunnel. In *42nd AIAA Fluid Dynamics Conference and Exhibit*. American Institute of Aeronautics and Astronautics.

BORG, M., KIMMEL, R. & STANFIELD, S. 2013 Traveling crossflow instability for HIFiRE-5 in a quiet hypersonic wind tunnel. In *43rd Fluid Dynamics Conference*. American Institute of Aeronautics and Astronautics.

CHERNORAY, V. G., DOVGAL, A. V., KOZLOV, V. V. & LOEFDAHL, L. 2005 Experiments on secondary instability of streamwise vortices in a swept-wing boundary layer. *J. Fluid Mech.* **534**, 295–325.

CORKE, T. C., ARNDT, A., MATLIS, E. H. & SEMPER, M. 2018 Control of stationary cross-flow modes in a Mach 6 boundary layer using patterned roughness. *J. Fluid Mech.* **856**, 822–849.

CORKE, T. C. & KNASIAK, K. F. 1998 Stationary travelling cross-flow mode interactions on a rotating disk. *J. Fluid Mech.* **355**, 285–315.

CORKE, T. C., MATLIS, E. H. & OTHMAN, H. 2007 Transition to turbulence in rotating-disk boundary layers – convective and absolute instabilities. *J. Engng Maths* **57**, 253–272.

CRAIG, S. & SARIC, W. S. 2016 Crossflow instability in a hypersonic boundary layer. *J. Fluid Mech.* **808**, 224–244.

CUMMINGS, R. & MCLAUGHLIN, T. 2012 Hypersonic Ludwieg tube design and future usage at the US Air Force Academy. In *50th AIAA Aerospace Sciences Meeting. AIAA Paper* 2012-0734.

ESTORF, M., WOLF, T. & RADESPIEL, R. 2005 Experimental and numerical investigations on the operation of the hypersonic Ludwieg tube Braunschweig. In *5th European Symposium on Aerothermodynamics for Space Vehicles*, ESA Special Publication, vol. 6, p. 579.

KING, R. A. 1992 Three-dimensional boundary-layer transition on a cone at Mach 3.5. *Exp. Fluids* **13**, 305–314.

LI, F., CHOUDHARI, M., CHANG, C.-L. & WHITE, J. 2010 Analysis of instabilities in non-axisymmetric hypersonic boundary layers over cones. In *10th AIAA/ASME Joint Thermophysics and Heat Transfer Conference. AIAA Paper* 2010-4643.

https://doi.org/10.1017/jfm.2020.15 Published online by Cambridge University Press

MALIK, M., LI, F. & CHANG, C.-L. 1994 Crossflow disturbances in three-dimensional boundary layers: nonlinear development, wave interaction and secondary instability. *J. Fluid Mech.* **268**, 1–36.

MALIK, M., LI, F., CHOUDHARI, M. & CHANG, C.-L. 1999 Secondary instability of crossflow vortices and swept-wing boundary-layer transition. *J. Fluid Mech.* **399**, 85–115.

MORKOVIN, M. V. 1990*a* *On Roughness-Induced Transition: Facts, Views & Speculation. Instability and Transition*, vol. I. Springer.

MORKOVIN, M. V. 1990*b* *Panel Summary on Roughness. Instability and Transition*, vol. I. Springer.

NEEL, I. T., LEIDY, A., TICHENOR, N. R. & BOWERSOX, R. D. 2018 Influence of environmental disturbances on hypersonic crossflow instability on the HIFiRE-5 elliptic cone. In *Presented at AIAA Scitech 2018*. American Institute of Aeronautics and Astronautics, paper number to be assigned.

PRESTON, J. 1954 The determination of turbulent skin friction by means of Pitot tubes. *J. R. Aero. Soc.* **14**, 109–121.

RADEZTSKY, R. H. JR, REIBERT, M. S. & SARIC, W. S. 1999 Effect of isolated micron-sized roughness on transition in swept-wing flows. *AIAA J.* **37** (11), 1370–1377.

REED, H. L. & SARIC, W. S. 1989 Stability of three-dimensional boundary layers. *Annu. Rev. Fluid Mech.* **21**, 235–284.

RESHOTKO, E. 2008 Paths to transition wall layers. In *Papers Presented During the EN-AVT-151-12 RTO AVT/VKI Lecture Series Held at the von Karman Institute, Rhode St. Gense, Belgium*. The von Karman Institute.

SARIC, W. S., CARILLO, R. C. & REIBERT, M. S. 1998 Leading-edge roughness as a transition control mechanism. *AIAA Paper* 98-0781.

SARIC, W. S. & REED, H. L. 2002 Supersonic laminar flow control on swept wings using distributed roughness. *AIAA Paper* 2002-0147.

SARIC, W. S., REED, H. L. & KERSCHEN, E. J. 2002 Boundary-layer receptivity to freestream disturbances. *Annu. Rev. Fluid Mech.* **34**, 291–319.

SARIC, W. S., REED, H. L. & WHITE, E. B. 2003 Stability and transition of three-dimensional boundary layers. *Annu. Rev. Fluid Mech.* **35**, 413–440.

SARIC, W. S., WEST, D. E., TUFTS, M. W. & REED, H. L. 2019 Experiments on discrete roughness element technology for swept-wing laminar flow control. *AIAA J.* **57** (2), 641–654.

SCHUELE, C.-Y. 2011 Control of sationary cross-flow modes in a Mach 3.5 boundary layer using passive and active roughness. PhD thesis, University of Notre Dame, Notre Dame, IN.

SCHUELE, C.-Y., CORKE, T. C. & MATLIS, E. H. 2013 Control of stationary cross-flow modes in a Mach 3.5 boundary layer using patterned passive and active roughness. *J. Fluid Mech.* **718**, 5–38.

WASSERMANN, P. & KLOKER, M. 2002 Mechanisms and passive control of crossflow-vortex-induced transition in three-dimensional boundary layer. *J. Fluid Mech.* **456**, 49–84.

WHITE, E. B. & SARIC, W. S. 2005 Secondary instability of crossflow vortices. *J. Fluid Mech.* **525**, 275–308.

https://doi.org/10.1017/jfm.2020.15 Published online by Cambridge University Press